

# SM3Det: A Unified Model for Multi-Modal Remote Sensing Object Detection

Yuxuan Li<sup>1</sup>    Xiang Li<sup>1,2†</sup>    Yunheng Li<sup>1</sup>    Yicheng Zhang<sup>1</sup>    Yimian Dai<sup>1</sup>  
 Qibin Hou<sup>1,2</sup>    Ming-Ming Cheng<sup>1,2</sup>    Jian Yang<sup>1†</sup>

<sup>1</sup> VCIP Lab, Computer Science, NKU    <sup>2</sup>NKIARI, Futian, Shenzhen    <sup>†</sup> Corresponding Authors  
 yuxuan.li.17@ucl.ac.uk, {xiang.li.implus, houqb, cmm, csjyang}@nankai.edu.cn  
 {yunhengli, zhangyc}@mail.nankai.edu.cn, yimian.dai@gmail.com

## Abstract

With the rapid advancement of remote sensing technology, high-resolution multi-modal imagery is now more widely accessible. Conventional Object detection models are trained on a single dataset, often restricted to a specific imaging modality and annotation format. However, such an approach overlooks the valuable shared knowledge across multi-modalities and limits the model’s applicability in more versatile scenarios. This paper introduces a new task called Multi-Modal Datasets and Multi-Task Object Detection (M2Det) for remote sensing, designed to accurately detect horizontal or oriented objects from any sensor modality. This task poses challenges due to 1) the trade-offs involved in managing multi-modal modelling and 2) the complexities of multi-task optimization. To address these, we establish a benchmark dataset and propose a unified model, **SM3Det** (**S**ingle **M**odel for **M**ulti-Modal datasets and **M**ulti-Task object **D**etection). SM3Det leverages a grid-level sparse MoE backbone to enable joint knowledge learning while preserving distinct feature representations for different modalities. Furthermore, it integrates a consistency and synchronization optimization strategy using dynamic learning rate adjustment, allowing it to effectively handle varying levels of learning difficulty across modalities and tasks. Extensive experiments demonstrate SM3Det’s effectiveness and generalizability, consistently outperforming specialized models on individual datasets. The code is available at <https://github.com/zcablii/SM3Det>.

## 1. Introduction

Remote sensing object detection [11, 13, 14, 37, 71, 74, 79, 86] typically involves multiple sensors employing different imaging mechanisms, resulting in diverse data modalities. Traditionally, detection models are developed for specific

datasets associated with a single modality and a predefined format detection task [10, 12, 40, 72], as shown in Figure 1 (b). This conventional approach overlooks the valuable and inherent joint knowledge within a unified remote sensing context. Furthermore, airborne platforms such as UAVs and satellites often carry multiple sensors, making it critical to process images from various modalities simultaneously. Previous multi-source object detection methods [47, 76, 83] have heavily relied on scarce, impractical, and inflexible spatially well-aligned paired images and spatial alignment algorithms [1, 5, 15]. These methods are also limited to performing single-format detection tasks, as depicted in Figure 1 (a). Thus, it is essential to develop a unified model capable of handling all modalities without requiring spatially aligned image pairs and performing multiple format detection tasks (referred to as “multi-tasks” throughout the paper), which is not thoroughly studied.

To fill this research gap, we propose a new task called Multi-Modal Datasets and Multi-Task Object Detection (M2Det). M2Det aims to detect objects in any given image, regardless of its modality, and across predefined detection tasks—whether horizontal bounding boxes or oriented bounding boxes—as illustrated in Figure 1 (c).

The M2Det task is closely related to two key research areas: multi-dataset object detection [63, 87] and multi-task learning [9, 82]. However, the M2Det task presents unique challenges. In traditional multi-dataset object detection, even though images may have different attributes—such as natural images and paintings—they often share similar underlying concepts (optical concepts). A simple joint training approach is effective, with a single model trained on the combined dataset typically outperforming models trained on individual datasets. In contrast, multi-modal datasets in remote sensing—such as RGB [59, 65], SAR [41, 78], IR [60], and multi-spectral images [19]—exhibit fundamentally different pattern concepts (as in Figure 6). While certain common knowledge may be shared across these modalities, the significant differences in data representation create

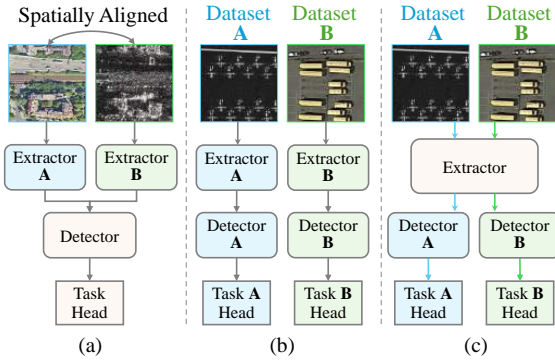


Figure 1. Comparison of tasks: (a) Spatially Aligned Multi-Modality, (b) Traditional Single Dataset, and (c) M2Det. M2Det aims to utilize a unified model for detecting objects in any modality, handling various detection tasks.

a substantial modality gap, complicating the integration of information across modalities. Additionally, remote sensing datasets often include diverse annotation types, such as horizontal [36, 41] and oriented [60, 65] bounding boxes, further adding complexity to model learning.

These challenges may impede traditional model learning and optimization in the following ways: **1) Representation Constraints:** A dense model that shares the same parameters across multiple tasks and modalities may encounter limitations in representation capacity, as a single set of parameters may struggle to effectively fit the diverse distributions inherent in each dataset. **2) Optimization Inconsistencies:** The varying learning difficulties across different modalities and tasks can lead to unsynchronized optimization rates or optimization directions for various components of the model. This inconsistency can result in conflicting optimization outcomes, adversely affecting the model’s ability to achieve different loss objectives.

To address these challenges, we first establish a comprehensive benchmark dataset by merging SARDet-100K [41], DOTA [65], and DroneVehicle [60], which collectively span SAR, optical, and infrared modalities. Subsequently, we propose a unified model, SM3Det, tailored for the M2Det task in remote sensing, addressing the challenges from both model architecture and model optimization perspectives:

**Model Architecture:** We propose integrating a plug-and-play grid-level sparse Mixture of Experts (MoE) architecture into backbone networks, enabling the model to capture both shared knowledge and modality-specific representations. Through dynamic routing, the experts operate on local spatial features, allowing the model to adaptively process information at a grid level, which is crucial for object detection tasks.

**Model Optimization:** We propose a novel Dynamic Learning Rate Adjustment (DLA) method that adaptively adjusts the learning rates of different network components with tailored policies. DLA accommodates the varying learning complexities across different tasks and modalities

by balancing the relative convergence rate and guaranteeing optimization direction consistency. Unlike traditional techniques that primarily modify loss weights or gradients—often lacking precise manipulation over specific network submodules or suffering from inefficiencies—our DLA provides fine-grained control while maintaining optimization efficiency.

The experiments indicate that our unified single SM3Det model significantly outperforms all individual models across all modality datasets. Our lightweight SM3Det variant not only demonstrates excellent performance but also features a substantially reduced number of parameters. Furthermore, the SM3Det model exhibits strong generalizability, enabling it to adapt to various backbones and detectors. Our contributions are summarized as follows:

- We introduce a new task: Multi-Modal Datasets and Multi-Task object detection in remote sensing using a unified detection model.
- We propose the SM3Det model, which addresses the challenges of the M2Det task by offering innovative solutions from both model architecture and model optimization perspectives.
- Extensive experiments and analyses on the established benchmark dataset demonstrate that our proposed single model is effective and outperforms individual models across all modalities.

## 2. Related Work

### 2.1. Multi-Dataset Object Detection

Multi-dataset object detection aims to leverage a diverse collection of datasets to learn general knowledge and achieve universal object detection. Leveraging multiple datasets in training has proven to be a highly effective strategy for enhancing the performance of deep learning models across various applications [31, 52, 69, 70, 85]. This approach has also been widely explored in the domain of object detection. The DA network [63], for instance, employs specialized SE layers [23] that serve as domain-specific attention mechanisms for individual datasets. Universal-RCNN [68] introduces a partitioned detector trained across multiple datasets, integrating features through an inter-dataset graph-based attention module. Unidet [87] advances this concept by proposing a unified label space and underscoring the importance of batch sampling strategies.

Models trained on combined optical-concept datasets typically outperform those trained on individual datasets, as multi-dataset training can serve as a powerful form of data augmentation. However, the diverse imaging modalities in remote sensing present unique challenges for joint training. This area remains largely unexplored.

## 2.2. Multi-Task Learning

Multi-task learning involves utilizing a single model to learn multiple objectives, typically with multiple task heads and loss functions. In multi-task learning, various strategies [9, 20, 32, 55] have been developed to address task imbalances and optimize learning outcomes. GradNorm [9] focuses on correcting gradient imbalances during backpropagation by adjusting the gradient sizes for each task’s loss function. Methods like Multi-Gradient Descent Algorithm [55] and PE-LTR [45] employ Pareto optimization for gradient backpropagation, though they can be inefficient due to the additional gradient calculations required. Similar to GradNorm, DWA [63] also uses task losses to assess convergence rates, however, it dynamically adjusts the weight of each task’s loss instead. Uncertainty [32] loss takes a different approach by incorporating homoscedastic uncertainty into the weighted loss function.

Unlike loss reweighting or gradient manipulation, our method dynamically adjusts the learning rate for network components, enhancing multi-modal datasets and multi-task learning by maintaining optimization consistency.

## 2.3. Mixture of Experts (MoE)

MoE [26, 27] leverages multiple expert networks to provide rich features. Sparse MoE[56] further introduces sparsity, allowing for the scaling up of model size without dramatically increasing computational complexity. In multi-task learning, sparse MoE enables different expert networks to learn distinct discriminative features. Most sparse MoE-based multi-task methods [8, 73, 73] are grounded in transformer architectures, integrating experts into vision transformer backbone blocks to selectively activate different paths during inference. DeepMoE [48] borrow the concept of sparse MoE into CNN networks by treating the channels within each convolutional layer as experts, enhancing representational power by adaptively sparsifying and recalibrating channel features. In multi-dataset learning, recent work [28] employs MoE within vision transformers to route image-level features to specialized experts.

However, sparse MoE for multi-modal datasets learning remains largely unexplored. Unlike prior methods that implement hard-coded, image-level routing [28, 63], we propose to leverage MoE into backbone networks at the feature grid level. This enables experts to effectively extract and process spatial features, learning both shared representations and distinct patterns across modalities.

# 3. Methods

## 3.1. Task Definition

The proposed M2Det task is designed to utilize a unified model for detecting interest objects in images from any modality, handling various predefined detection tasks, such

as horizontal and rotated bounding boxes. The significance of this task is evident in various real-world applications, including low-altitude economy [24, 30], low-altitude aerial surveillance [4, 6], earth observation [3, 35], and other research domains [2, 25, 29, 33]. For instance, drones and satellites equipped with M2Det models can fully leverage available multi-modal data while benefiting from simplified version control and the seamless integration of multiple sensors without requiring model updates on the device. Furthermore, processing images of different modalities in a single model within one mini-batch maximizes the parallel computing capabilities of GPUs, thereby enhancing computational and energy efficiency on edge devices.

## 3.2. Methodological Overview

The overall network architecture follows the classic design of multi-task learning models [63, 87]. It consists of a relatively heavy feature space shared component (backbone) and relatively lightweight feature space independent components (task heads). The backbone is responsible for joint representation learning, with most parameters being shared, thus ensuring parameter efficiency. The lightweight heads are separated to accommodate distinct features and task learning. However, as discussed in Section 1, modality and task gaps may degrade the performance of such classic multi-task models. To address this issue, we propose the SM3Det model, which consists of two parts:

**Model architecture:** A sparse MoE backbone where experts are activated on local image features of multi-modality dataset images at the grid level.

**Model optimization:** An efficient dynamic learning rate adjustment method, to handle the varying learning difficulties and optimization inconsistency across multiple tasks and modalities.

## 3.3. Grid-level MoE

Previous approaches to multi-dataset object detection [68, 87] utilize dense models that leverage shared concepts among datasets to enhance joint knowledge representation. In the case of multi-modal remote sensing images, this joint knowledge also exists [41], though it may be less explicit, with common weak cues such as shape and scale across modalities. However, due to inherent modality and task gaps, employing a dense model that utilizes the same parameters across multiple tasks and modalities can result in a congested feature/representation space, ultimately reducing the model’s expressiveness. Therefore, it is essential to explore methods that leverage joint knowledge across modalities while enabling distinct representation learning for each modality to prevent feature space interference.

Drawing inspiration from the success of Sparse MoE networks [56], which are characterized by their sparsity and high capacity, we propose leveraging MoE for the

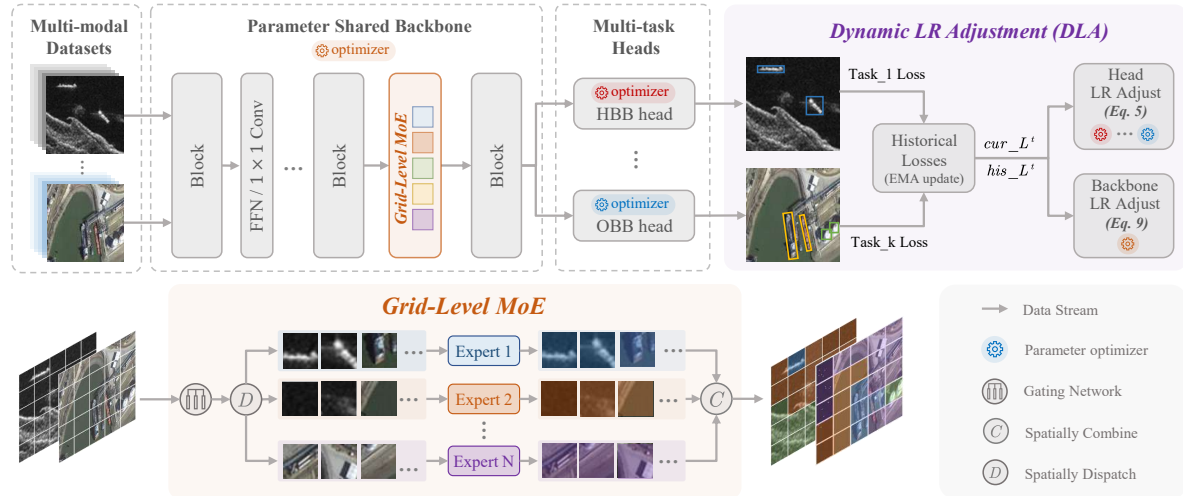


Figure 2. A conceptual illustration of SM3Det model. “HBB”: horizontal bounding box, “OBB”: oriented bounding box.

M2Det task. For transformer-based backbones like Swin-Transformer [49] or PVT [62], we integrate MoE experts within the FFN components. For modern CNNs [21, 39, 50], which often employ  $1 \times 1$  convolutions [43] for feature interaction or dimensionality reduction/expansion, we introduce sparse experts to enhance these layers. Unlike previous transformer-based detectors that route an entire image’s features through a single expert [28], our design allows experts to operate on local grid features within the backbone. This approach ensures that experts process similar spatial patterns across modalities, facilitating shared representation learning. Simultaneously, multiple experts capture distinct patterns across modalities, enabling independent representation learning. Specifically, for the local spatial input feature  $x_{ij}$  at the  $i$ -th row and  $j$ -th column of a deep image feature, the output feature  $f_{MoE}(x_{ij})$  after the MoE layer is:

$$f_{MoE}(x_{ij}) = \sum_{n=1}^N G(x_{ij}) \cdot Conv_n^{1 \times 1}(x_{ij}), \quad (1)$$

$$G(x_{ij}) = \text{TOP}_k \left( \text{Softmax} \left( \frac{E^T W x_{ij}}{\tau \|W x_{ij}\| \|E\|} \right) \right), \quad (2)$$

where  $N$  is the total number of experts,  $G$  is the gating function and  $Conv_n^{1 \times 1}$  is the  $n$ -th  $1 \times 1$  convolutional expert. Each expert has a representation embedding in the matrix  $E$ . The input feature  $x$  is first transformed by the matrix  $W$ . The product of  $Wx$  is then compared with each expert embedding in  $E$  to calculate the similarity. This comparison is then normalized by the product of the norms of  $Wx$  and  $E$ , ensuring the similarities are scale-invariant. The similarity scores are passed through a *Softmax* function, converting them into a probability distribution. This means the gating function assigns a probability to each expert, indicating its relevance to the input feature  $x$ . Finally, the  $\text{TOP}_k$  operator selects the top- $k$  experts with the highest probabilities.

It reweights each expert by assigning the *Softmax* probability to the top- $k$  experts, setting the rest to zero. This step sparsifies the model by focusing only on a small subset of experts, reducing computational complexity and enhancing the model’s expressiveness to handle diverse tasks and modalities.

In summary,  $f_{MoE}(x_{ij})$  is a weighted sum of the outputs from top- $k$  experts. The weights are determined by the gating function  $G$ , which dynamically selects the most relevant expert(s) for each local feature. The MoE creates a sparser feature space in the backbone model. By focusing on local patterns, the model can learn independently to model multiple modalities and local object patterns. Our design effectively addresses the challenges of crowded feature spaces and enhances the expressiveness of the model.

In practical implementation, to fully utilize the pre-trained backbone weights, we initialize the weights of added experts by duplicating the corresponding pretrained  $1 \times 1$  convolutional layers’ weights before downstream model fine-tuning, ensuring all experts can be evenly chosen at the beginning of fine-tuning. For the task heads, we maintain simplicity and adhere to the existing design of task heads as in [32, 63, 87].

### 3.4. Dynamic Learning Rate Adjustment (DLA)

In multi-modal, multi-dataset, and multi-task object detection tasks, one primary challenge is the varying learning difficulties [9, 32] across modalities and tasks. The variation can cause unsynchronized optimization rates and inconsistent optimization directions [51], leading to conflicting objectives among different loss functions. To address this problem, we propose a novel Dynamic Learning Rate Adjustment method (DLA) to manage the differing learning difficulties across tasks and modalities.

DLA takes the losses from each task head as indicators to determine the current convergence rate of each task and

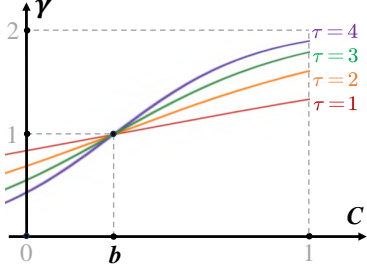


Figure 3. Reweighting curves for various temperature values ( $\tau$ ).

the overall optimization direction of the network, adjusting the learning rate (LR) accordingly. Specifically, one policy is used for the LR of each task head (non-shared network) to balance the relative convergence rate of each task, and another policy is used for the backbone (network with shared weights) to ensure consistency in the optimization direction.

We denote the training loss from the iteration  $i$  of task  $t$  as  $cur\_L_i^t$ . Each task’s loss maintains an exponential moving average (EMA) value as the smoothed historical statistic, denoted as  $his\_L_i^t$ , i.e.,

$$his\_L_i^t = \alpha \cdot cur\_L_i^t + (1 - \alpha) \cdot his\_L_{i-1}^t. \quad (3)$$

**For the head’s LR adjustment**, we use the ratio of  $his\_L$  to  $cur\_L$  as the inverse of the convergence rate for iteration  $i$  of task  $t$  as:

$$w_i^t = \frac{his\_L_i^t}{cur\_L_i^t}. \quad (4)$$

The *Softmax* with temperature  $\theta$  is then used to reweight the LR of the corresponding network task head, aiming to balance the convergence speed of each task. The reweighting factor  $\lambda_i^t$  for task  $t$  at training iteration  $i$  is denoted as:

$$\lambda_i^t = \frac{T \cdot e^{w_i^t/\theta}}{\sum_k^T e^{w_i^k/\theta}}, \quad (5)$$

where  $T$  is the total number of tasks. As a result, a relatively large value of  $cur\_L_i^t$  indicates faster convergence for task  $t$ , leading to a smaller  $w_i^t$  and, consequently, a lower reweighting factor  $\lambda_i^t$  to prevent overly rapid convergence. Conversely, a smaller value of  $cur\_L_i^t$  results in a larger  $\lambda_i^t$ . This strategy ensures that the convergence rate of each task remains balanced throughout training.

**For the backbone’s LR adjustment**, the reweighting is based on the historical consistency of each loss. To measure the training convergence consistency, we define a consistency score  $C$  based on  $cur\_L$  and  $his\_L$ . Specifically,  $cur\_L$  and  $his\_L$  are first converted into probability distributions using the function  $P$ , which employs a simple *Softmax* function:

$$P(L) = Softmax(L), \quad (6)$$

Next, the Kullback-Leibler divergence,  $D_{KL}$ , is calculated to evaluate whether the current losses from each task remain stable and consistent with their historical values:

$$C = 1 - D_{KL}(P(cur\_L) \parallel P(his\_L)) \quad (7)$$

$$= 1 - \sum_t^T P(cur\_L^t) \cdot \log \frac{P(cur\_L^t)}{P(his\_L^t)}, \quad (8)$$

therefore  $C$  is in the range of  $(-\infty, 1]$ . A larger  $C$  indicates that the relative values of the current iteration losses are similar to their historical values, suggesting that the current batch of samples stabilizes the network updates. In this case, the LR has to be increased to make the network converge faster. Conversely, a lower  $C$  indicates instability, suggesting that the current samples make some tasks more difficult and others easier to learn compared to the previous average state. If the network updates the shared weights too aggressively in such cases, the network will be optimized in the direction of the harder task of the current iteration, which might harm the easier tasks. Therefore, the network should update cautiously to reduce the LR.

To balance this, we propose dynamically reweighting the shared weight backbone with the following policy:

$$\gamma_i = 2 \cdot Sigmoid((C - b) \cdot \tau) \quad (9)$$

$$= \frac{2}{1 + e^{-(C-b) \cdot \tau}}. \quad (10)$$

The scalar factor of 2 ensures the reweighted value after the sigmoid function is in the range of  $(0, 2)$ .  $b$  is the hyperparameter, bias, which can be interpreted as the reweighting threshold, i.e. when the  $C$  is  $b$ , the reweight is 1.  $\tau$  is the temperature for value sensitivity adjustment. The reweighting curves for various temperatures and the relation between  $b$  and  $C$  are demonstrated in Figure 3.

## 4. Experiments and Analysis

### 4.1. Dataset

To train and evaluate models for the M2Det task, we establish a new benchmark dataset by merging three detection datasets: SARDet-100K [41], DOTA-v1.0 [65], and DroneVehicle [60], which correspond to SAR, optical, and infrared modalities, respectively. We refer to this combined dataset as the SOI-Det dataset.

The **SARDet-100K** [41] dataset is a SAR object detection dataset containing six object categories: Aircraft, Ship, Car, Bridge, Tank, and Harbor. The dataset consists of 94,493 training images with 198,747 instances, and 11,613 testing images with 24,023 instances. All annotations are provided as horizontal bounding boxes (HBB). **DOTA** [65] is an optical aerial object detection dataset that includes 15 categories. After splitting each image into  $800 \times 800$  patches with a 400-pixel overlap, the dataset yields 25,028

training images containing 337,728 instances, and 17,041 testing images with 95,380 instances. All annotations are in the form of oriented bounding boxes (OBB). To avoid the severe dataset imbalance in the merged SOI-Det dataset, we use only a subset of SARDet-100K. For more details please refer to the Supplementary Material. **DroneVehicle** [60] is an infrared vehicle detection dataset with 5 categories: car, truck, bus, van, and freight car. The images are sized at  $640 \times 512$  pixels. The dataset consists of 17,990 training images with 316,411 instances, and 8,980 testing images with 159,616 instances. Similar to DOTA-v1.0, all annotations are in the form of OBB.

## 4.2. Implementation Details

For each dataset, we evaluate using the mean Average Precision at IoU thresholds 0.5 (@50), at IoU thresholds 0.75 (@75), and at IoU thresholds from 0.5 to 0.95 (mAP). Additionally, we report the overall mAP across the three datasets to assess overall performance.

For individual dataset training, models are trained for 12 epochs using the AdamW optimizer. In multi-modal joint training, we ensure that the total number of iterations matches the combined iterations of individual dataset training for fairness. In the main results and ablation studies, ConvNext-T is used as the default backbone unless otherwise specified. All FLOPs reported in this paper are calculated using an  $800 \times 800$  image input. More implementation details can be found in the **Supplementary Material**.

## 4.3. Main Results

We evaluate the performance of our proposed SM3Det model against individual dataset training, simple joint training, and three SOTA methods that can be adapted for this task: UniDet [87] with a partitioned head, the DA network [63] implemented within the ConvNext-T backbone, and uncertainty loss [32] implemented upon UniDet. The main results are presented in Table 1.

It can be observed that simple joint training of the three multi-modality datasets—i.e., merely merging the datasets and using a model with a shared backbone and separate task heads, along with a random data sampling strategy—results in a significant performance drop. This phenomenon highlights the increased challenge of this task compared to multi-dataset training for general object detection, where simple joint training typically enhances the performance of individual datasets [63, 87]. The previous SOTA methods, UniDet, DA and uncertainty loss, barely exceed the baseline by a small margin. In contrast, our proposed SM3Det model significantly improves overall mAP performance from 48.23 to 50.20, an increase of 1.97 mAP. To be noticed, our lightweight version of SM3Det which only incorporates DLA but without MoE structures, also easily outperforms other SOTA methods.

Model	FLOPs	#P	Test on	mAP	@50	@75
3 models	403G	126M	Overall	48.23	79.39	51.26
GFL [38]	131G	36M	SARDet-100K	57.31	87.44	61.99
O-RCNN[67]	136G	45M	DOTA	45.31	77.70	46.45
O-RCNN[67]	136G	45M	DroneVehicle	46.09	74.78	52.79
Simple Joint Training [68]	403G	66M	Overall	47.05	77.56	50.11
			SARDet-100K	53.46	84.11	57.29
			DOTA	45.18	76.37	46.78
			DroneVehicle	44.99	73.28	51.50
DA [63] +ConvNext-T	403G	66M	Overall	48.37	79.76	51.66
			SARDet-100K	53.86	84.93	58.09
			DOTA	46.23	78.47	47.58
			DroneVehicle	48.21	77.43	56.16
UniDet [87] (Partitioned)	403G	66M	Overall	48.47	79.55	52.01
			SARDet-100K	53.81	84.70	57.43
			DOTA	46.49	78.28	48.59
			DroneVehicle	47.99	77.17	55.74
Uncertainty loss [32]	403G	66M	Overall	48.79	79.99	52.50
			SARDet-100K	53.43	84.81	57.41
			DOTA	46.94	78.73	49.08
			DroneVehicle	48.78	77.96	56.88
SM3Det (DLA only)	403G	66M	Overall	49.40	80.19	52.93
			SARDet-100K	58.54	88.59	62.67
			DOTA	46.18	77.86	47.95
			DroneVehicle	48.09	77.09	56.20
SM3Det	487G	178M	Overall	50.20	80.68	53.79
			SARDet-100K	60.64	89.94	65.06
			DOTA	46.47	77.88	48.24
			DroneVehicle	48.87	77.99	56.90

Table 1. Model performance comparison on the SOI-Det dataset (SARDet-100K + DOTA + DroneVehicle). The proposed SM3Det model outperforms individual models and other SOTA models.

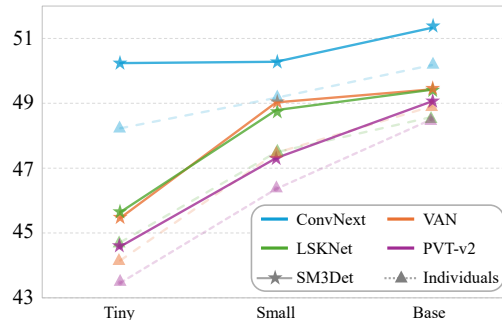


Figure 4. Generalization of SM3Det on different CNN backbones.

To assess the generalization capability of SM3Det, we evaluate its performance across different backbones and detectors. As illustrated in Figure 4, SM3Det significantly outperforms individual models across various modern convolutional backbones, including ConvNext [50], VAN [21], LSKNet [39] and PVT-v2 [62]. The model also exhibits reasonable scalability as the model size increases. Additionally, we evaluate SM3Det with different detectors. For simplicity, since both the optical dataset (DOTA) and the infrared dataset (DroneVehicle) involve OBB regression tasks, we use the same head network structure in our model.

Stage 1	Stage 2	Stage 3	Stage 4	FLOPs	#P	mAP	@50	@75
None	None	None	None	403G	66M	48.51	79.70	51.78
None	None	None	Even	422G	132M	48.85+(0.34)	80.07(+0.37)	51.86+(0.08)
None	None	Even	Even	469G	174M	49.31+(0.80)	80.26+(0.56)	52.84+(1.06)
None	Even	Even	Even	487G	178M	<b>49.53+(1.02)</b>	<b>80.47+(0.77)</b>	<b>53.06+(1.28)</b>
Even	Even	Even	Even	506G	179M	49.47+(0.96)	80.33+(0.63)	52.98+(1.20)
All	All	All	All	572G	249M	49.30+(0.79)	80.23+(0.53)	53.03+(1.25)

Table 2. Experiments on spatial MoE with different MoE layer positions. “None”: no MoE layers, “Even”: MoE added to even-indexed layers, and “All”: MoE added to all layers within the stage. Each MoE layer comprises 8 experts with a top-2 selection. Selectively incorporating MoE layers in the even-indexed layers of the last three stages enhances model performance.

MoE ( $N, k$ )	w/o MoE	2, 2	4, 2	6, 2	8, 2	10, 2	8, 1	8, 2	8, 3	3, 1 Image-Level	3, 1 Grid-Level
FLOPs (G)	403	469	469	469	469	469	403	469	531	403	403
#P (M)	66	82	113	142	174	205	174	174	174	98	98
mAP	48.51	48.94	49.11	49.13	<b>49.31</b>	49.24	49.05	<b>49.31</b>	49.13	48.49	<b>48.60</b>
@50	79.70	80.25	80.10	79.74	<b>80.26</b>	80.18	79.72	<b>80.26</b>	79.98	79.60	<b>79.67</b>
@75	51.78	52.01	52.13	52.76	52.84	52.79	52.30	52.84	<b>52.77</b>	51.51	<b>52.06</b>

Table 3. Experiments on the MoE backbone with varying numbers of experts and top- $k$  selection configurations. Experts are applied only to the even-indexed layers of the last two stages for validation efficiency.  $N$ : number of experts to add.  $k$ : number of experts to activate. The optimal configuration balancing performance and computational efficiency is identified as 8 experts with a top- $k$  value of 2.

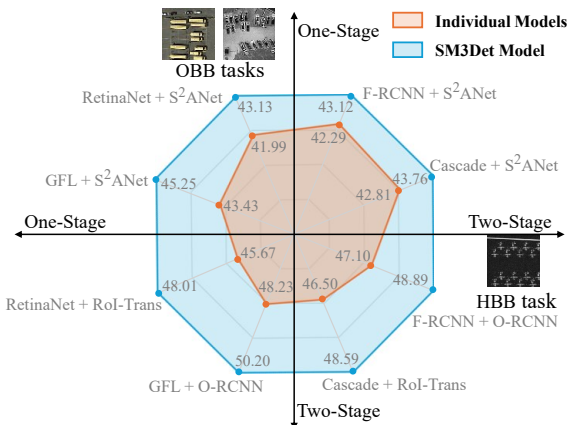


Figure 5. Generalization of SM3Det on different detector heads.

In contrast, for the SAR dataset (SARDet-100K), which involves an HBB regression task, we implement a standard horizontal object detection head. Figure 5 shows our evaluation of SM3Det on one-stage (RetinaNet [44], GFL [38] and S<sup>2</sup>ANet [22]) and two-stage (F-RCNN [53], Cascade F-RCNN [7], O-RCNN [67] and RoI-Transformer [16]) detector combinations. The results consistently demonstrate that SM3Det significantly outperforms individual models across all detector combinations.

#### 4.4. Ablation Study and Analysis

**MoE Layer Positions.** We conduct an ablation study to assess the impact of incorporating MoE layers at different stages of the ConvNext backbone. As shown in Table 2, selectively adding MoE layers in the last three stages enhances model performance, resulting in a 1.02% mAP improvement with a manageable increase in computational cost. This enhancement likely results from the richer se-

mantic information in deeper stages, allowing experts to specialize more effectively. Conversely, adding MoE layers to all stages or every layer within each stage does not lead to optimal performance, indicating that overusing MoE may introduce optimization challenges, as also highlighted in recent studies [34, 54].

**Expert Number and top- $k$  Number.** In sparse MoE architecture, the number of experts to add ( $N$ ) and the top- $k$  value play crucial roles in determining the model’s performance and efficiency. Increasing  $N$  generally enhances the model’s representation capacity, while a higher top- $k$  value allows for more specialized knowledge to be applied to each input. However, these enhancements come at the cost of a larger model size, increased computational complexity, and potentially requiring more training data to ensure that each expert is adequately trained. Therefore, selecting the appropriate number of experts and top- $k$  value is critical for achieving an optimal balance between model performance and computational efficiency. The results in Table 3 underscore the importance of tuning the number of experts and the top- $k$  value in a sparse MoE architecture. It reveals that the optimal configuration for this sparse MoE architecture in terms of balancing performance and computational efficiency is 8 experts with a top-2 experts. This configuration maximizes the model’s ability to learn from diverse inputs without introducing unnecessary complexity or overfitting.

**Image-level v.s. Grid-level MoE.** In Table 3, the grid-level MoE outperforms the image-level counterpart, indicating that grid-level experts more effectively capture spatial variations across different objects in multi-modal images. By processing features at a finer spatial granularity, experts are more attuned to object localization, making grid-level MoE particularly well-suited for object detection tasks.

**Grid-level Experts Visualization.** To better understand the

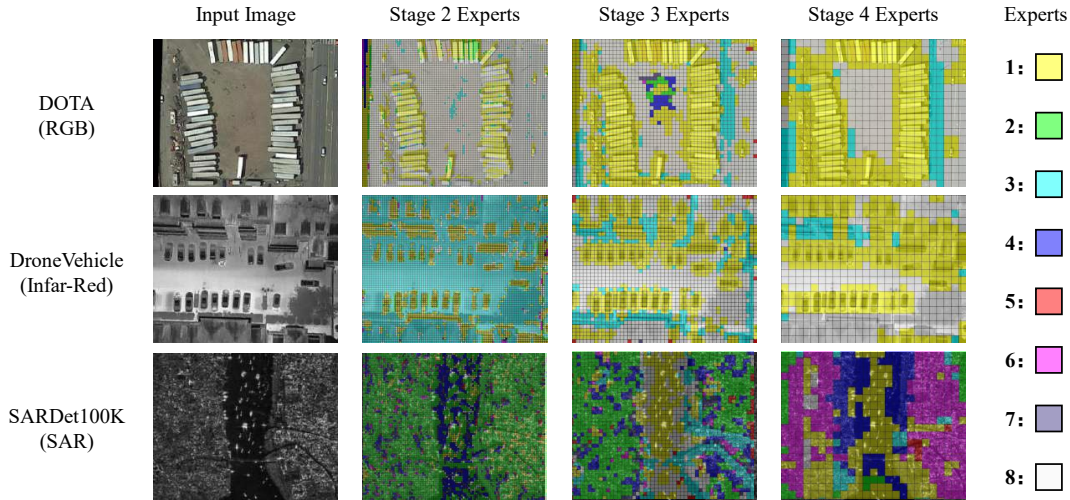


Figure 6. Visualization of grid expert activation across the last three stages of a well-tuned backbone on SAR, RGB, and IF images. Each square grid represents the receptive field at a given stage, with different colors indicating the local grid areas processed by distinct experts. The top-1 selected experts for each grid are shown. Each expert specializes in processing unique local patterns and semantics.

$\tau, b$	3, 0.3	3, 0.4	3, 0.5	3, 0.6	2, 0.4	3, 0.4	4, 0.4	w/o DLA	w/o Head policy	w/o Backbone policy
<b>mAP</b>	50.14	<b>50.20</b>	50.07	50.03	49.92	<b>50.20</b>	50.03	49.47	49.86	50.11
@50	80.61	<b>80.68</b>	80.66	80.61	80.55	<b>80.68</b>	80.44	80.33	80.53	80.66
@75	<b>53.81</b>	53.79	54.00	53.98	53.56	53.79	53.79	52.98	53.44	53.70

Table 4. Experiments on the DLA method with varying temperature ( $\tau$ ) and bias ( $b$ ). DLA is not sensitive to bias  $b$ .  $\tau = 3$  and  $b = 0.4$  achieves the best performance, effectively managing learning rate adjustments across diverse tasks and datasets.

grid-level expert selection behaviour for different modal images, we visualize the selection results for each grid area across the last three stages of a well-tuned ConvNext-T backbone. In this visualization, each square grid represents the corresponding receptive field of that stage, with local deep features processed by different experts indicated by distinct colours. The top-1 selected experts are illustrated in Figure 6. For both RGB and IR images, a consistent pattern emerges: expert 1 predominantly processes salient objects, while Expert 3 focuses on background patches across all three stages. In contrast, the situation is more complex for SAR images. Particularly at stage 4, three experts (Expert 1, Expert 4, and Expert 6) are responsible for processing background areas, with Expert 1 also handling ship objects. Additional visualizations and detailed MoE behaviour analysis can be found in the **Supplementary Material**.

**DLA hyperparameters.** We conduct an ablation study on each component of the proposed DLA method, as well as the sensitivity of its two key hyperparameters. The results are summarized in Table 4. Omitting the learning rate adjustment for either the head or backbone leads to significant performance degradation. The bias parameter  $b$  and temperature  $\tau$  dynamically adjust learning rates to account for varying task and modality difficulties. Specifically,  $b$  serves as a reweighting balance point, meaning when the calculated consistency score equals  $b$ , the reweighting factor is 1. A bias value of  $b = 0.4$  proved optimal when the tempera-

ture was fixed at 3, striking a good balance in learning rate adjustments. Notably, variations in  $b$  did not significantly impact performance, indicating that the method is robust to changes in bias. Regarding temperature,  $\tau$ , influences the reweighting curve in both the network head and the backbone’s learning rate adjustment strategy. Larger values result in sharper, more sensitive adjustments. A temperature of  $\tau = 3$  provided the best balance between stability and responsiveness. In summary, the  $\tau = 3$  and  $b = 0.4$  yielded the best performance, effectively managing learning rate adjustments across diverse tasks and datasets.

## 5. Limitation and Future Work

An important modality in remote sensing is multi-spectrum imaging. However, due to the limited availability of large-scale multi-spectrum object detection datasets, we could not include such datasets in our experiments. Our model designs and observations can extend beyond remote sensing. They can be applied to other scenarios involving multiple modalities or the joint training of diverse datasets. Potential applications include medical imaging [17] (e.g., X-Ray, NMR, and CT) and autonomous driving [18] (e.g., camera, LiDAR, and Radar). These applications present exciting avenues for future research.



## 6. Conclusion

In conclusion, this paper introduces a new and challenging task of Multi-Modal Datasets and Multi-Task Object Detection in remote sensing. To tackle this, we developed the SM3Det model, integrating a novel grid-level MoE approach and a dynamic learning rate adjustment strategy. Intensive experiments and thorough analysis demonstrate SM3Det’s strong performance and generalizability.

## References

- [1] Tofael Ahamed, Lei Tian, Yanshui Jiang, Bin Zhao, Hx Liu, and Kuan Chong Ting. Tower remote-sensing system for monitoring energy crops; image acquisition and geometric corrections. *Biosystems engineering*, 112(2):93–107, 2012. 1
- [2] Ramón Alcarria, Borja Bordel, Miguel Angel Manso, Teresa Iturrioz, and Marina Pérez. Analyzing uav-based remote sensing and wsn support for data fusion. In *Proceedings of the International Conference on Information Technology & Systems*, 2018. 3
- [3] Katherine Anderson, Barbara Ryan, William Sonntag, Argyro Kavvada, and Lawrence Friedl. Earth observation in service of the 2030 agenda for sustainable development. *Geo-spatial Information Science*, 2017. 3
- [4] Danilo Avola, Luigi Cinque, Angelo Di Mambro, Anxhelo Diko, Alessio Fagioli, Gian Luca Foresti, Marco Raoul Marini, Alessio Mecca, and Daniele Pannone. Low-altitude aerial video surveillance via one-class svm anomaly detection from textural features in uav images. *Information*, 2021. 3
- [5] Seunghwan Ban and Taejung Kim. Precise relative geometric correction for multi-sensor satellite images. *The International Archives of the Photogrammetry, Remote Sensing and Spatial Information Sciences*, 48:17–23, 2024. 1
- [6] Ilker Bozcan and Erdal Kayacan. Au-air: A multi-modal unmanned aerial vehicle dataset for low altitude traffic surveillance. In *2020 IEEE International Conference on Robotics and Automation*, 2020. 3
- [7] Zhaowei Cai and Nuno Vasconcelos. Cascade R-CNN: Delving into high quality object detection. In *CVPR*, 2018. 7, 4
- [8] Tianlong Chen, Xuxi Chen, Xianzhi Du, Abdullah Rashwan, Fan Yang, Huizhong Chen, Zhangyang Wang, and Yeqing Li. Adamv-moe: Adaptive multi-task vision mixture-of-experts. In *ICCV*, 2023. 3
- [9] Zhao Chen, Vijay Badrinarayanan, Chen-Yu Lee, and Andrew Rabinovich. Gradnorm: Gradient normalization for adaptive loss balancing in deep multitask networks. In *ICML*, 2018. 1, 3, 4
- [10] Yimian Dai and Yiquan Wu. Reweighted infrared patch-tensor model with both nonlocal and local priors for single-frame small target detection. *IEEE journal of selected topics in applied earth observations and remote sensing*, 2017. 1
- [11] Yimian Dai, Yiquan Wu, Fei Zhou, and Kobus Barnard. Asymmetric contextual modulation for infrared small target detection. In *WACV*, 2021. 1
- [12] Yimian Dai, Yiquan Wu, Fei Zhou, and Kobus Barnard. Attentional local contrast networks for infrared small target detection. *TGRS*, 2021. 1
- [13] Yimian Dai, Peiwen Pan, Yulei Qian, Yuxuan Li, Xiang Li, Jian Yang, and Huan Wang. Pick of the bunch: Detecting infrared small targets beyond hit-miss trade-offs via selective rank-aware attention. *TGRS*, 2024. 1
- [14] Yimian Dai, Minrui Zou, Yuxuan Li, Xiang Li, Kang Ni, and Jian Yang. Denodet: Attention as deformable multi-subspace feature denoising for target detection in sar images. *arXiv*, 2024. 1
- [15] Chabitha Devaraj and Chintan A Shah. Automated geometric correction of landsat mss 11g imagery. *IEEE Geoscience and Remote Sensing Letters*, 11(1):347–351, 2013. 1
- [16] Jian Ding, Nan Xue, Yang Long, Gui-Song Xia, and Qikai Lu. Learning RoI transformer for oriented object detection in aerial images. In *CVPR*, 2019. 7, 4
- [17] Aarthipoornima Elangovan and Thangaraja Jeyaseelan. Medical imaging modalities: a survey. In *International Conference on emerging trends in engineering, technology and science*, 2016. 8
- [18] Di Feng, Christian Haase-Schütz, Lars Rosenbaum, Heinz Hertlein, Claudius Glaeser, Fabian Timm, Werner Wiesbeck, and Klaus Dietmayer. Deep multi-modal object detection and semantic segmentation for autonomous driving: Datasets, methods, and challenges. *IEEE Transactions on Intelligent Transportation Systems*, 2020. 8
- [19] The International Society for Photogrammetry and Remote Sensing (ISPRS). 2D semantic labeling contest - Potsdam. <https://www.isprs.org/education/benchmarks/UrbanSemLab/2d-sem-label-potsdam.aspx>, 2022. 1
- [20] Michelle Guo, Albert Haque, De-An Huang, Serena Yeung, and Li Fei-Fei. Dynamic task prioritization for multitask learning. In *ECCV*, 2018. 3
- [21] Meng-Hao Guo, Chengrou Lu, Zheng-Ning Liu, Ming-Ming Cheng, and Shiyong Hu. Visual attention network. *Computational Visual Media*, 2022. 4, 6
- [22] Jiaming Han, Jian Ding, Jie Li, and Gui-Song Xia. Align deep features for oriented object detection. *TGRS*, 2020. 7, 4
- [23] Jie Hu, Li Shen, and Gang Sun. Squeeze-and-excitation networks. In *CVPR*, 2018. 2
- [24] Changqing Huang, Shifeng Fang, Hua Wu, Yong Wang, and Yichen Yang. Low-altitude intelligent transportation: system architecture, infrastructure, and key technologies. *Journal of Industrial Information Integration*, page 100694, 2024. 3
- [25] Yoshio Inoue. Satellite-and drone-based remote sensing of crops and soils for smart farming—a review. *Soil Science and Plant Nutrition*, 2020. 3
- [26] Robert A Jacobs and Michael I Jordan. Learning piecewise control strategies in a modular neural network architecture. *IEEE Transactions on Systems, Man, and Cybernetics*, 1993. 3
- [27] Robert A Jacobs, Michael I Jordan, Steven J Nowlan, and Geoffrey E Hinton. Adaptive mixtures of local experts. *Neural computation*, 1991. 3

- [28] Yash Jain, Harkirat Behl, Zsolt Kira, and Vibhav Vineet. Damex: Dataset-aware mixture-of-experts for visual understanding of mixture-of-datasets. *NeurIPS*, 2024. 3, 4
- [29] Ole B Jensen. Drone city–power, design and aerial mobility in the age of “smart cities”. *Geographica Helvetica*, 2016. 3
- [30] Yihang Jiang, Xiaoyang Li, Guangxu Zhu, Hang Li, Jing Deng, and Qingjiang Shi. 6g non-terrestrial networks enabled low-altitude economy: Opportunities and challenges. *arXiv preprint arXiv:2311.09047*, 2023. 3
- [31] Georgios Kapidis, Ronald Poppe, and Remco C Veltkamp. Multi-dataset, multitask learning of egocentric vision tasks. *TPAMI*, 2021. 2
- [32] Alex Kendall, Yarin Gal, and Roberto Cipolla. Multi-task learning using uncertainty to weigh losses for scene geometry and semantics. In *CVPR*, 2018. 3, 4, 6
- [33] Asif Khan, Evsen Yanmaz, and Bernhard Rinner. Information merging in multi-uav cooperative search. In *2014 IEEE international conference on robotics and automation*, 2014. 3
- [34] Bo Li, Yifei Shen, Jingkan Yang, Yezhen Wang, Jiawei Ren, Tong Che, Jun Zhang, and Ziwei Liu. Sparse mixture-of-experts are domain generalizable learners. In *ICLR*, 2023. 7
- [35] Deren Li, Mi Wang, Zhipeng Dong, Xin Shen, and Lite Shi. Earth observation brain (eob): An intelligent earth observation system. *Geo-spatial information science*, 2017. 3
- [36] Ke Li, Gang Wan, Gong Cheng, Liqiu Meng, and Junwei Han. Object detection in optical remote sensing images: A survey and a new benchmark. *ISPRS*, 2020. 2
- [37] Weijie Li, Wei Yang, Tianpeng Liu, Yuenan Hou, Yuxuan Li, Zhen Liu, Yongxiang Liu, and Li Liu. Predicting gradient is better: Exploring self-supervised learning for sar atr with a joint-embedding predictive architecture. *ISPRS Journal o*, 2024. 1
- [38] Xiang Li, Chengqi Lv, Wenhai Wang, Gang Li, Lingfeng Yang, and Jian Yang. Generalized focal loss: Towards efficient representation learning for dense object detection. *TPAMI*, 2022. 6, 7, 4
- [39] Yuxuan Li, Qibin Hou, Zhaohui Zheng, Ming-Ming Cheng, Jian Yang, and Xiang Li. Large selective kernel network for remote sensing object detection. In *ICCV*, 2023. 4, 6
- [40] Yuxuan Li, Xiang Li, Yimain Dai, Qibin Hou, Li Liu, Yongxiang Liu, Ming-Ming Cheng, and Jian Yang. Lsknet: A foundation lightweight backbone for remote sensing. *arXiv preprint arXiv:2403.11735*, 2024. 1
- [41] Yuxuan Li, Xiang Li, Weijie Li, Qibin Hou, Li Liu, Ming-Ming Cheng, and Jian Yang. Sardet-100k: Towards open-source benchmark and toolkit for large-scale sar object detection. In *NeurIPS*, 2024. 1, 2, 3, 5
- [42] Zechao Li, Yanpeng Sun, Liyan Zhang, and Jinhui Tang. Ctnet: Context-based tandem network for semantic segmentation. *TPAMI*, 2022. 4
- [43] M Lin. Network in network. *arXiv*, 2013. 4
- [44] Tsung-Yi Lin, Priya Goyal, Ross Girshick, Kaiming He, and Piotr Dollár. Focal loss for dense object detection. In *ICCV*, 2017. 7, 4
- [45] Xiao Lin, Hongjie Chen, Changhua Pei, Fei Sun, Xuanji Xiao, Hanxiao Sun, Yongfeng Zhang, Wenwu Ou, and Peng Jiang. A pareto-efficient algorithm for multiple objective optimization in e-commerce recommendation. In *Proceedings of ACM Conference on recommender systems*, 2019. 3
- [46] Xin Lin, Bo Zhang, Fan Wu, Chao Wang, Yali Yang, and Huiqin Chen. Sived: A sar image dataset for vehicle detection based on rotatable bounding box. *Remote Sensing*, 2023. 1
- [47] Jinming Liu, Hao Chen, and Yu Wang. Multi-source remote sensing image fusion for ship target detection and recognition. *Remote Sensing*, 13(23):4852, 2021. 1
- [48] Jiang-Jiang Liu, Qibin Hou, Ming-Ming Cheng, Changhu Wang, and Jiashi Feng. Improving convolutional networks with self-calibrated convolutions. In *CVPR*, 2020. 3
- [49] Ze Liu, Yutong Lin, Yue Cao, Han Hu, Yixuan Wei, Zheng Zhang, Stephen Lin, and Baining Guo. Swin transformer: Hierarchical vision transformer using shifted windows. In *CVPR*, 2021. 4
- [50] Zhuang Liu, Hanzi Mao, Chao-Yuan Wu, Christoph Feichtenhofer, Trevor Darrell, and Saining Xie. A convnet for the 2020s. In *CVPR*, 2022. 4, 6
- [51] Akihiro Nakano, Shi Chen, and Kazuyuki Demachi. Cross-task consistency learning framework for multi-task learning. *arXiv*, 2021. 4
- [52] René Ranftl, Katrin Lasinger, David Hafner, Konrad Schindler, and Vladlen Koltun. Towards robust monocular depth estimation: Mixing datasets for zero-shot cross-dataset transfer. *TPAMI*, 44(3):1623–1637, 2020. 2
- [53] Shaoqing Ren, Kaiming He, Ross Girshick, and Jian Sun. Faster R-CNN: Towards real-time object detection with region proposal networks. In *NeurIPS*, 2015. 7, 4
- [54] Carlos Riquelme, Joan Puigcerver, Basil Mustafa, Maxim Neumann, Rodolphe Jenatton, André Susano Pinto, Daniel Keysers, and Neil Houlsby. Scaling vision with sparse mixture of experts. *NeurIPS*, 2021. 7
- [55] Ozan Sener and Vladlen Koltun. Multi-task learning as multi-objective optimization. *Advances in neural information processing systems*, 2018. 3
- [56] Noam Shazeer, Azalia Mirhoseini, Krzysztof Maziarz, Andy Davis, Quoc Le, Geoffrey Hinton, and Jeff Dean. Outrageously large neural networks: The sparsely-gated mixture-of-experts layer. *arXiv preprint arXiv:1701.06538*, 2017. 3
- [57] Zhuo Su, Jiehua Zhang, Longguang Wang, Hua Zhang, Zhen Liu, Matti Pietikäinen, and Li Liu. Lightweight pixel difference networks for efficient visual representation learning. *TPAMI*, 2023. 4
- [58] Shuzhou Sun, Shuaifeng Zhi, Qing Liao, Janne Heikkilä, and Li Liu. Unbiased scene graph generation via two-stage causal modeling. *TPAMI*, 2023. 4
- [59] Xian Sun, Peijin Wang, Zhiyuan Yan, Feng Xu, Ruiping Wang, Wenhui Diao, Jin Chen, Jihao Li, Yingchao Feng, Tao Xu, Martin Weinmann, Stefan Hinz, Cheng Wang, and Kun Fu. FAIR1M: A benchmark dataset for fine-grained object recognition in high-resolution remote sensing imagery. *ISPRS*, 2022. 1

- [60] Yiming Sun, Bing Cao, Pengfei Zhu, and Qinghua Hu. Drone-based rgb-infrared cross-modality vehicle detection via uncertainty-aware learning. *IEEE Transactions on Circuits and Systems for Video Technology*, pages 1–1, 2022. [1](#), [2](#), [5](#), [6](#)
- [61] Chao Wang, Rui Ruan, Zhicheng Zhao, Chenglong Li, and Jin Tang. Category-oriented localization distillation for sar object detection and a unified benchmark. *IEEE Transactions on Geoscience and Remote Sensing*, 2023. [1](#)
- [62] Wenhai Wang, Enze Xie, Xiang Li, Deng-Ping Fan, Kaitao Song, Ding Liang, Tong Lu, Ping Luo, and Ling Shao. Pvt v2: Improved baselines with pyramid vision transformer. *Computational Visual Media*, 2022. [4](#), [6](#)
- [63] Xudong Wang, Zhaowei Cai, Dashan Gao, and Nuno Vasconcelos. Towards universal object detection by domain attention. In *CVPR*, 2019. [1](#), [2](#), [3](#), [4](#), [6](#)
- [64] Shunjun Wei, Xiangfeng Zeng, Qizhe Qu, Mou Wang, Hao Su, and Jun Shi. Hrsid: A high-resolution sar images dataset for ship detection and instance segmentation. *IEEE Access*, 2020. [1](#)
- [65] Gui-Song Xia, Xiang Bai, Jian Ding, Zhen Zhu, Serge Belongie, Jiebo Luo, Mihai Datcu, Marcello Pelillo, and Liangpei Zhang. DOTA: A large-scale dataset for object detection in aerial images. In *CVPR*, 2018. [1](#), [2](#), [5](#)
- [66] Runfan Xia, Jie Chen, Zhixiang Huang, Huiyao Wan, Bocai Wu, Long Sun, Baidong Yao, Haibing Xiang, and Mengdao Xing. Ctrtransar: A visual transformer based on contextual joint representation learning for sar ship detection. *Remote Sensing*, 2022. [1](#)
- [67] Xingxing Xie, Gong Cheng, Jiabao Wang, Ke Li, Xiwen Yao, and Junwei Han. Oriented r-cnn and beyond. *IJCV*, 2024. [6](#), [7](#), [1](#), [4](#)
- [68] Hang Xu, Linpu Fang, Xiaodan Liang, Wenxiong Kang, and Zhenguo Li. Universal-rcnn: Universal object detector via transferable graph r-cnn. In *AAAI*, 2020. [2](#), [3](#), [6](#)
- [69] Ke Yan, Jinzheng Cai, Youjing Zheng, Adam P Harrison, Dakai Jin, Youbao Tang, Yuxing Tang, Lingyun Huang, Jing Xiao, and Le Lu. Learning from multiple datasets with heterogeneous and partial labels for universal lesion detection in ct. *IEEE Transactions on Medical Imaging*, 2020. [2](#)
- [70] Gengshan Yang, Joshua Manela, Michael Happold, and Deva Ramanan. Hierarchical deep stereo matching on high-resolution images. In *CVPR*, 2019. [2](#)
- [71] Xue Yang, Junchi Yan, Ziming Feng, and Tao He. R3det: Refined single-stage detector with feature refinement for rotating object. In *Proceedings of the AAAI conference on artificial intelligence*, 2021. [1](#)
- [72] Xue Yang, Junchi Yan, Qi Ming, Wentao Wang, Xiaopeng Zhang, and Qi Tian. Rethinking rotated object detection with Gaussian Wasserstein distance loss. In *ICML*, 2021. [1](#)
- [73] Yuqi Yang, Peng-Tao Jiang, Qibin Hou, Hao Zhang, Jinwei Chen, and Bo Li. Multi-task dense prediction via mixture of low-rank experts. In *CVPR*, 2024. [3](#)
- [74] Yi Yu, Xue Yang, Qingyun Li, Yue Zhou, Feipeng Da, and Junchi Yan. H2rbox-v2: Incorporating symmetry for boosting horizontal box supervised oriented object detection. *NeurIPS*, 2024. [1](#)
- [75] Dong Zhang, Hanwang Zhang, Jinhui Tang, Xian-Sheng Hua, and Qianru Sun. Causal intervention for weakly-supervised semantic segmentation. *NeurIPS*, 2020. [4](#)
- [76] Hongkang Zhang, Shao-Lun Huang, and Ercan Engin Kuruoglu. Hgr correlation pooling fusion framework for recognition and classification in multimodal remote sensing data. *Remote Sensing*, 16(10):1708, 2024. [1](#)
- [77] Peng Zhang, Hao Xu, Tian Tian, Peng Gao, Linfeng Li, Tianming Zhao, Nan Zhang, and Jinwen Tian. Sefepnet: Scale expansion and feature enhancement pyramid network for sar aircraft detection with small sample dataset. *IEEE Journal of Selected Topics in Applied Earth Observations and Remote Sensing*, 2022. [1](#)
- [78] Tianwen Zhang, Xiaoling Zhang, Jianwei Li, Xiaowo Xu, Baoyou Wang, Xu Zhan, Yanqin Xu, Xiao Ke, Tianjiao Zeng, Hao Su, et al. Sar ship detection dataset (ssdd): Official release and comprehensive data analysis. *Remote Sensing*, 2021. [1](#)
- [79] Wenhua Zhang, Licheng Jiao, Yuxuan Li, Zhongjian Huang, and Haoran Wang. Laplacian feature pyramid network for object detection in vhr optical remote sensing images. *TGRS*, 2022. [1](#)
- [80] Wenhua Zhang, Licheng Jiao, Fang Liu, Shuyuan Yang, and Jia Liu. Dfat: Dynamic feature-adaptive tracking. *IEEE Transactions on Circuits and Systems for Video Technology*, 2023. [4](#)
- [81] Wenhua Zhang, Wenjing Deng, Zhen Cui, Jia Liu, and Licheng Jiao. Object knowledge distillation for joint detection and tracking in satellite videos. *TGRS*, 2024. [4](#)
- [82] Yu Zhang and Qiang Yang. A survey on multi-task learning. *IEEE transactions on knowledge and data engineering*, 2021. [1](#)
- [83] Zenghui Zhang, Limeng Zhang, Juanping Wu, and Weiwei Guo. Optical and synthetic aperture radar image fusion for ship detection and recognition: Current state, challenges, and future prospects. *IEEE Geoscience and Remote Sensing Magazine*, 2024. [1](#)
- [84] Penghai Zhao, Qinghua Xing, Kairan Dou, Jinyu Tian, Ying Tai, Jian Yang, Ming-Ming Cheng, and Xiang Li. From words to worth: Newborn article impact prediction with llm. *arXiv*, 2024. [4](#)
- [85] Xiangyun Zhao, Samuel Schultze, Gaurav Sharma, Yi-Hsuan Tsai, Manmohan Chandraker, and Ying Wu. Object detection with a unified label space from multiple datasets. In *2020*, 2020. [2](#)
- [86] Jie Zhou, Chao Xiao, Bo Peng, Zhen Liu, Li Liu, Yongxiang Liu, and Xiang Li. Diffdet4sar: Diffusion-based aircraft target detection network for sar images. *TGRS Letters*, 2024. [1](#)
- [87] Xingyi Zhou, Vladlen Koltun, and Philipp Krähenbühl. Simple multi-dataset detection. In *CVPR*, 2022. [1](#), [2](#), [3](#), [4](#), [6](#)

# SM3Det: A Unified Model for Multi-Modal Remote Sensing Object Detection

## Supplementary Material

### A. Implementation Details

For each dataset, we evaluate using the mean Average Precision at IoU thresholds 0.5 (@50), at IoU thresholds 0.75 (@75), and at IoU thresholds from 0.5 to 0.95 (mAP). Additionally, we report the overall mAP across the three datasets to assess overall performance.

To avoid the severe dataset imbalance in the merged SOI-Det dataset, we use only a subset of SARDet-100K: HRSID [64], MSAR [66], SADD [77], OGSOD [61], and SIVED [46]. This subset of SARDet-100K includes 47,097 training images with 125,462 annotated instances and 4,481 testing images with 12,566 instances. During training, each batch is sampled uniformly across the three datasets—SARDet-100K, DOTA, and DroneVehicle—in a 2:1:1 ratio, ensuring that each dataset is cycled through approximately once every 20K iterations.

All models are fine-tuned on their respective training sets. For SARDet-100K and DroneVehicle, models are evaluated on the corresponding test sets, while for the DOTA dataset, evaluation is conducted on the validation set. For individual dataset training, models are trained for 12 epochs using the AdamW optimizer.

In multi-modal joint training, we ensure that the total number of iterations matches the combined iterations of individual dataset training for fairness. Each batch employs uniform sampling from the three datasets (SARDet-100K, DOTA, and DroneVehicle) with a ratio of 2:1:1, ensuring that all datasets are cycled through approximately once every 20K iterations. Following previous network designs [63, 87], we share the backbone network and use separate task heads for different datasets and tasks. Specifically, after feature extraction by the backbone network, features from SARDet-100K images are passed to the GFL head (due to its superior performance on horizontal SAR object detection [41]), while those from DOTA and DroneVehicle are passed to two individual O-RCNN [67] heads (due to the high-performance of O-RCNN on oriented object detection).

In the main results and ablation studies, ConvNext-T is used as the default backbone unless otherwise specified. The initial learning rate is set to 0.0001, with a weight decay of 0.05. Model training is conducted using 8 RTX 3090 GPUs, with a batch size of 4 per GPU. All FLOPs reported in this paper are calculated using an 800×800 image input.

### B. Detailed Experiment Results

#### B.1 Ablation study on MoE configurations

We investigate the impact of different configurations of the sparse MoE architecture on model performance. Specifically, we analyze variations in the number of experts and the Top-K value, which determines the number of experts activated for each input. The detailed results are given in Table S5.

As the number of experts increases from 2 to 10 with a fixed Top-K value of 2, there is a consistent improvement in overall mAP scores until reaching 8 experts. This suggests that up to a certain point, adding more experts allows the model to better capture diverse patterns in the data, leading to improved detection performance across multiple datasets. When the number of experts is increased to 10, the overall mAP slightly decreases to 49.24. This indicates that while adding more experts can enhance model capacity, there may be diminishing returns or even a negative impact when the number of experts exceeds the capacity of the training data to sufficiently train them all.

When examining the impact of the Top-K value, it is clear that setting Top-K to 2 generally provides a good balance between performance and computational demand.

For example, with 8 experts and a Top-K value of 2, the overall mAP is 49.31, which is higher than both the Top-K values of 1 and 3. A Top-K value of 1, while less computationally intensive, results in a slightly lower mAP of 49.05, indicating that activating only one expert per input may limit the model’s capacity to leverage the diverse expertise available. Conversely, increasing the Top-K value to 3, while introducing more computational demands, does not improve performance, as the overall mAP drops to 49.13.

This suggests that activating only one expert per input may limit the model’s capacity to leverage the diverse expertise available, while activating too many experts for a single input may lead to over-complexity without corresponding benefits, potentially causing interference between experts or inefficient use of computational resources.

In summary, the ablation study reveals that the optimal configuration for this sparse MoE architecture in terms of balancing performance and computational efficiency is 8 experts with a Top-K value of 2. This configuration maximizes the model’s ability to learn from diverse inputs without introducing unnecessary complexity or overfitting.

#### B.2 Ablation on DLA Hyperparameters

We conduct an ablation study to evaluate the sensitivity of two key hyperparameters—temperature ( $\tau$ ) and bias

MoE Cfg	FLOPs	#P	Test	mAP	@50	@75
w/o MoE	403G	66M	Overall	48.51	79.70	51.78
			SARDet-100K	56.99	87.32	61.41
			DOTA	45.59	77.86	47.01
			DroneVehicle	47.09	76.10	54.53
Experts: 2 Top: 2	469G	82M	Overall	48.94	80.25	52.01
			SARDet-100K	57.81	88.33	61.96
			DOTA	45.89	78.34	47.15
			DroneVehicle	47.42	76.28	54.65
Experts: 4 Top: 2	469G	113M	Overall	49.11	80.10	52.13
			SARDet-100K	58.52	88.39	62.47
			DOTA	45.84	77.99	46.98
			DroneVehicle	47.64	76.49	55.17
Experts: 6 Top: 2	469G	143M	Overall	49.11	79.74	52.76
			SARDet-100K	59.16	88.89	64.10
			DOTA	45.42	76.94	47.15
			DroneVehicle	48.14	77.14	56.00
Experts: 8 Top: 2	469G	174M	Overall	49.31	80.26	52.84
			SARDet-100K	58.99	88.89	63.87
			DOTA	45.69	77.64	47.13
			DroneVehicle	48.53	77.74	56.71
Experts: 10 Top: 2	469G	205M	Overall	49.24	80.18	52.79
			SARDet-100K	59.24	89.11	63.78
			DOTA	45.65	77.54	47.27
			DroneVehicle	48.02	77.37	56.17
Experts: 8 Top: 1	403G	174M	Overall	49.05	79.72	52.30
			SARDet-100K	59.10	88.60	63.97
			DOTA	45.23	76.88	46.31
			DroneVehicle	48.44	77.60	56.28
Experts: 8 Top: 2	469G	174M	Overall	49.31	80.26	52.84
			SARDet-100K	58.99	88.89	63.87
			DOTA	45.69	77.64	47.13
			DroneVehicle	48.53	77.74	56.71
Experts: 8 Top: 3	531G	174M	Overall	49.13	79.98	52.77
			SARDet-100K	59.18	88.98	63.65
			DOTA	45.43	77.32	47.33
			DroneVehicle	48.16	77.15	56.05
Image-level Experts: 3 Top: 1	403G	98M	Overall	48.49	79.60	51.51
			SARDet-100K	56.88	87.17	60.49
			DOTA	45.56	77.74	46.94
			DroneVehicle	47.21	76.07	54.45
Grid level Experts: 3 Top: 1	403G	98M	Overall	48.60	79.67	52.06
			SARDet-100K	56.51	87.23	61.00
			DOTA	45.80	77.90	47.51
			DroneVehicle	47.50	75.93	54.96

Table S5. Experiments on grid-level MoE with varying numbers of experts and top-K selection configurations. Experts are applied only to the even-indexed layers of the last two stages for validation efficiency.

(b)—in the proposed DLA method, which dynamically adjusts learning rates to accommodate varying learning difficulties across tasks and modalities. The detailed results are

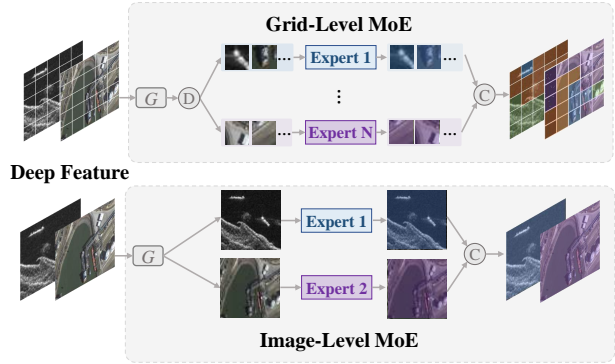


Figure S7. Illustration of the Grid-level and Image-level Sparse MoE. A comparison of these two designs is provided in Table S5, where the grid-level MoE demonstrates superior performance over the image-level MoE on the M2Det task.

given in Table S6.

The bias parameter  $b$  serves as a reweighting balance point. When the consistency score equals  $b$ , the reweighting factor is 1. Our analysis shows that a bias value of  $b = 0.4$  yields optimal performance, particularly when  $\tau$  is set to 3, achieving an overall mean Average Precision (mAP) of 50.20%. This configuration also leads to the highest performance on the SARDet-100K dataset (60.64% mAP) and DroneVehicle (49.03% mAP). Variations in bias from 0.3 to 0.5 result in marginal performance changes, indicating robustness to bias adjustments.

Regarding temperature,  $\tau$  shapes the reweighting curve, affecting how sensitive learning rates adapt. A temperature of  $\tau = 3$  strikes an ideal balance between stability and responsiveness, as evidenced by the peak overall mAP. Lowering  $\tau$  to 2 decreases the overall mAP to 49.92% and impairs task performance. Conversely, increasing  $\tau$  to 4 results in a slight decline to 50.03%, suggesting that excessive smoothing or sharpening hinders the model’s ability to react to varying task difficulties.

In summary, the combination of  $\tau = 3$  and  $b = 0.4$  yields the best performance, effectively managing learning rate adjustments across diverse tasks and datasets. This study highlights the importance of tuning these hyperparameters to optimize the DLA method’s capabilities in multi-modal object detection scenarios.

T	b	Test	mAP	@50	@75
w/o DLA		Overall	49.47	80.33	52.98
		SARDet-100K	58.97	88.82	63.40
		DOTA	46.02	77.84	47.73
		DroneVehicle	48.41	77.62	56.23
3	0.3	Overall	50.14	80.61	53.81
		SARDet-100K	60.86	90.02	66.01
		DOTA	46.23	77.68	47.81
		DroneVehicle	49.03	77.99	56.90
3	0.4	Overall	50.20	80.68	53.79
		SARDet-100K	60.64	89.94	65.06
		DOTA	46.47	77.88	48.24
		DroneVehicle	48.87	77.99	56.90
3	0.5	Overall	50.07	80.66	54.00
		SARDet-100K	60.77	90.04	65.74
		DOTA	46.11	77.70	48.16
		DroneVehicle	49.11	78.28	57.43
3	0.6	Overall	50.03	80.61	53.98
		SARDet-100K	60.49	89.92	65.30
		DOTA	46.19	77.68	48.39
		DroneVehicle	48.98	78.11	57.14
2	0.4	Overall	49.92	80.55	59.56
		SARDet-100K	60.95	90.71	65.90
		DOTA	45.85	77.35	47.81
		DroneVehicle	48.89	77.98	87.05
3	0.4	Overall	50.20	80.68	53.79
		SARDet-100K	60.64	89.94	65.06
		DOTA	46.47	77.88	48.24
		DroneVehicle	48.87	77.99	56.90
4	0.4	Overall	50.03	80.44	53.79
		SARDet-100K	61.23	90.59	66.32
		DOTA	45.86	77.13	47.58
		DroneVehicle	49.08	78.19	57.39

Table S6. Experiments on the DLA method with varying temperature ( $\tau$ ) and bias ( $b$ ).

### B.3 Detailed results on different backbones

The performance of SM3Det across various backbones, including ConvNext, VAN, LSKNet, and PVT-v2, demonstrates its robustness and adaptability in different scenarios. As shown in Table S7, S8 and S9, SM3Det consistently outperforms individual models in terms of mean Average Precision (mAP) across all datasets. Specifically, SM3Det shows a notable improvement in overall mAP, particularly at higher IoU thresholds (@50 and @75), indicating its effectiveness in precise object detection tasks.

Among the evaluated backbones, SM3Det paired with the ConvNext-B backbone achieved the highest overall mAP of 51.33% with a strong performance across all individual datasets, particularly SARDet-100K where it attained a mAP of 65.20%. This indicates that the backbone’s advanced feature extraction capabilities, when combined with SM3Det, significantly enhance detection accuracy. Similarly, SM3Det with VAN-B and LSKNet-B yield competitive results, with overall mAPs of 49.43% and 49.42%, respectively, further showcasing the model’s scalability and generalization capabilities.

These results confirm that SM3Det not only scales effectively with larger backbone models but also generalizes well across different architectural designs, making it a versatile solution for various object detection tasks in remote sensing.

### B.3 Detailed results on different detectors

Based on the results presented in Table S11, the SM3Det framework consistently outperforms individual models across all evaluated detector combinations. The performance improvement is evident in both one-stage (GFL [38], Retina [44], S<sup>2</sup>ANet [22]) and two-stage (F-RCNN [53], Cascade F-RCNN [7], RoI-Trans [16], O-RCNN [67]) detectors, where SM3Det achieves higher mAP scores, particularly at higher IoU thresholds (@75). These results underscore the effectiveness of SM3Det’s architecture in leveraging the strengths of multiple detectors, leading to superior object detection performance across diverse datasets like SARDet-100K, DOTA, and DroneVehicle. The overall mAP improvements further validate the robustness of SM3Det in enhancing detection accuracy.

### C. Grid-level sparse MoE analysis

Visualization of grid expert activation across the last three stages of a well-tuned ConvNext-T backbone on SARDet-100K, DOTA, and DroneVehicle images are given in Figure S8, S9, S10. Each square grid represents the receptive field at a given stage, with different colours indicating the local grid areas processed by distinct experts. The top-1 selected experts for each grid are shown.

In addition to the visualization, we further analyze the

Backbone	Model	Test	mAP	@50	@75
ConvNext-T	individual models	Overall	48.23	79.39	51.26
		SARDet-100K	57.31	87.44	61.99
		DOTA	45.31	77.70	46.45
	DroneVehicle	Overall	46.09	74.78	52.79
		SARDet-100K	60.64	89.94	65.06
		DOTA	46.47	77.88	48.24
	SM3Det	Overall	50.24	80.68	53.81
		SARDet-100K	60.64	89.94	65.06
		DOTA	46.47	77.88	48.24
ConvNext-S	individual models	Overall	49.17	80.06	52.31
		SARDet-100K	60.62	89.54	64.85
		DOTA	45.24	77.71	45.45
	DroneVehicle	Overall	47.22	75.72	54.82
		SARDet-100K	62.98	91.49	68.77
		DOTA	45.33	76.03	46.98
	SM3Det	Overall	50.28	80.13	54.30
		SARDet-100K	62.98	91.49	68.77
		DOTA	45.33	76.03	46.98
ConvNext-B	individual models	Overall	50.18	80.53	53.75
		SARDet-100K	62.27	90.40	66.87
		DOTA	46.02	77.79	47.73
	DroneVehicle	Overall	48.14	76.89	56.05
		SARDet-100K	65.20	92.41	70.02
		DOTA	45.86	76.35	48.10
	SM3Det	Overall	51.33	80.77	55.51
		SARDet-100K	65.20	92.41	70.02
		DOTA	45.86	76.35	48.10
DroneVehicle	Overall	51.09	80.07	60.34	
	SARDet-100K	65.20	92.41	70.02	
	DOTA	45.86	76.35	48.10	

Table S7. Performance comparison of SM3Det with individual models across different ConvNext backbone scales.

behaviour of sparse MoE expert selection at the dataset scale. We pass all test images from SARDet-100K, DOTA, and DroneVehicle datasets through the well-trained SM3Det model and gather statistics on expert participation. Specifically, the participation of an expert in a given MoE layer is quantified by the softmax probability of the gate function in Eq. 2. The statistical results, presented in Figure S11, These findings validate the advantage of our sparse MoE design in addressing the M2Det task. The expert selection patterns demonstrate that some experts contribute to shared representation learning across all three modalities, while others specialize in distinct patterns, activating only specific modalities. This balance supports both joint and independent representation learning. Notably, experts activated by SAR images typically show low activation in the other two modalities, indicating that SAR images utilize a distinct set of experts. In contrast, Infrared and RGB images share several highly activated experts, reflecting greater overlap in their representations. This observation aligns with the conventional understanding that SAR imagery embodies unique concepts and characteristics distinct from those in other modalities.

Backbone	Model	Test	mAP	@50	@75	
VAN-T	individual models	Overall	44.15	75.21	46.77	
		SARDet-100K	46.74	77.63	49.71	
		DOTA	43.31	75.36	44.73	
		DroneVehicle	43.55	71.86	49.38	
	SM3Det	Overall	45.46	76.28	48.37	
		SARDet-100K	49.28	80.85	52.08	
		DOTA	43.60	74.73	45.22	
		DroneVehicle	46.47	75.43	53.37	
		<hr/>				
		VAN-S	individual models	Overall	47.47	78.78
SARDet-100K	52.71			83.82	57.74	
DOTA	45.47			77.67	46.91	
DroneVehicle	74.17			76.07	54.27	
SM3Det	Overall		49.03	79.60	52.76	
	SARDet-100K		57.98	88.36	62.46	
	DOTA		45.50	76.66	47.37	
	DroneVehicle		48.87	77.91	57.31	
	<hr/>					
	VAN-B		individual models	Overall	48.91	79.99
SARDet-100K		53.73		84.89	58.11	
DOTA		47.42		79.24	49.86	
DroneVehicle		47.58		76.38	55.42	
SM3Det		Overall	49.43	80.57	53.34	
		SARDet-100K	56.82	87.82	61.15	
		DOTA	46.62	78.58	48.92	
		DroneVehicle	48.98	77.82	57.24	

Table S8. Performance comparison of SM3Det with individual models across different **VAN** backbone scales.

Backbone	Model	Test	mAP	@50	@75	
LSKNet-T	individual models	Overall	44.71	75.86	47.31	
		SARDet-100K	47.24	78.24	50.39	
		DOTA	43.93	75.97	45.25	
		DroneVehicle	44.00	72.67	49.78	
	SM3Det	Overall	45.64	76.89	48.25	
		SARDet-100K	49.95	81.76	53.61	
		DOTA	43.56	75.44	44.17	
		DroneVehicle	46.71	75.42	54.04	
		<hr/>				
		LSKNet-S	individual models	Overall	47.49	78.65
SARDet-100K	53.12			84.33	57.64	
DOTA	45.46			77.36	47.73	
DroneVehicle	46.80			75.72	54.01	
SM3Det	Overall		48.79	79.78	52.42	
	SARDet-100K		58.41	88.48	62.83	
	DOTA		44.80	76.69	46.61	
	DroneVehicle		49.20	78.63	57.36	
	<hr/>					
	LSKNet-B		individual models	Overall	48.58	79.43
SARDet-100K		54.00		84.81	58.46	
DOTA		46.87		78.45	48.76	
DroneVehicle		47.19		75.91	51.35	
SM3Det		Overall	49.42	80.34	53.31	
		SARDet-100K	56.70	87.75	60.93	
		DOTA	46.61	78.11	48.94	
		DroneVehicle	49.13	78.14	57.29	

Table S9. Performance comparison of SM3Det with individual models across different **LSKNet** backbone scales.



Backbone	Model	Test	mAP	@50	@75
PVT-v2 T	individual models	Overall	43.46	75.33	45.39
		SARDet-100K	47.63	78.83	50.96
		DOTA	41.81	74.79	42.18
		DroneVehicle	43.39	72.73	48.36
	SM3Det	Overall	44.58	76.43	46.81
		SARDet-100K	48.58	80.71	52.31
		DOTA	42.72	75.39	42.92
		DroneVehicle	45.38	74.43	51.86
PVT-v2 S	individual models	Overall	46.36	78.38	49.61
		SARDet-100K	52.01	84.24	57.19
		DOTA	44.28	77.14	45.60
		DroneVehicle	45.84	75.08	52.54
	SM3Det	Overall	47.31	79.21	50.08
		SARDet-100K	54.53	85.48	58.94
		DOTA	44.37	77.53	45.01
		DroneVehicle	47.47	76.71	54.66
PVT-v2 B	individual models	Overall	48.51	80.23	52.05
		SARDet-100K	56.04	87.00	61.27
		DOTA	45.55	78.41	46.92
		DroneVehicle	48.37	77.54	56.39
	SM3Det	Overall	49.34	80.72	53.05
		SARDet-100K	57.34	87.75	62.24
		DOTA	46.24	78.81	47.92
		DroneVehicle	49.06	78.02	57.41

Table S10. Performance comparison of SM3Det with individual models across different **PVT-v2** backbone scales.

Detectors	Model	Test	mAP	@50	@75
SARDet-100K: GFL DOTA: O-RCNN DroneVehicle: O-RCNN	individual models	Overall	48.23	79.39	51.26
		SARDet-100K	57.31	87.44	61.99
		DOTA	45.31	77.70	46.45
	SM3Det	DroneVehicle	46.09	74.78	52.79
		Overall	50.20	80.68	53.81
		SARDet-100K	60.64	89.94	65.06
SARDet-100K: Retina DOTA: RoI-Trans DroneVehicle: RoI-Trans	individual models	DOTA	46.47	77.88	48.24
		DroneVehicle	48.87	77.99	56.90
		Overall	45.67	77.92	47.22
	SM3Det	SARDet-100K	51.08	82.50	55.27
		DOTA	43.93	77.37	43.10
		DroneVehicle	44.42	74.06	49.94
SARDet-100K: F-RCNN DOTA: O-RCNN DroneVehicle: O-RCNN	individual models	Overall	48.01	78.83	51.35
		SARDet-100K	53.04	83.99	57.76
		DOTA	45.43	76.79	46.50
	SM3Det	DroneVehicle	49.69	78.76	58.23
		Overall	47.10	78.61	50.17
		SARDet-100K	52.40	84.09	57.28
SARDet-100K: Cascade DOTA: RoI-Trans DroneVehicle: RoI-Trans	individual models	DOTA	45.31	77.70	46.45
		DroneVehicle	46.09	74.78	52.79
		Overall	48.89	79.39	53.20
	SM3Det	SARDet-100K	54.56	85.62	59.83
		DOTA	46.09	76.80	48.38
		DroneVehicle	50.50	79.69	59.68
SARDet-100K: Cascade DOTA: S <sup>2</sup> ANet DroneVehicle: S <sup>2</sup> ANet	individual models	Overall	46.50	78.32	48.24
		SARDet-100K	54.65	84.26	59.66
		DOTA	43.93	77.37	43.10
	SM3Det	DroneVehicle	44.42	74.06	49.94
		Overall	48.59	79.04	51.69
		SARDet-100K	56.30	85.39	61.46
SARDet-100K: F-RCNN DOTA: S <sup>2</sup> ANet DroneVehicle: S <sup>2</sup> ANet	individual models	DOTA	45.00	76.46	45.23
		DroneVehicle	50.11	79.16	59.32
		Overall	42.29	77.18	40.68
	SM3Det	SARDet-100K	52.40	84.09	57.28
		DOTA	38.47	75.81	32.82
		DroneVehicle	41.64	72.98	44.35
SARDet-100K: Cascade DOTA: S <sup>2</sup> ANet DroneVehicle: S <sup>2</sup> ANet	individual models	Overall	43.12	77.40	42.83
		SARDet-100K	49.20	81.68	53.13
		DOTA	39.92	76.20	35.87
	SM3Det	DroneVehicle	45.44	75.85	51.33
		Overall	42.81	77.22	41.23
		SARDet-100K	54.65	84.26	59.66
SARDet-100K: GFL DOTA: S <sup>2</sup> ANet DroneVehicle: S <sup>2</sup> ANet	individual models	DOTA	38.47	75.81	32.82
		DroneVehicle	41.64	72.98	44.35
		Overall	43.76	77.28	43.63
	SM3Det	SARDet-100K	53.11	82.73	57.98
		DOTA	39.51	75.61	35.32
		DroneVehicle	45.27	75.76	51.32
SARDet-100K: GFL DOTA: S <sup>2</sup> ANet DroneVehicle: S <sup>2</sup> ANet	individual models	Overall	43.43	77.95	41.77
		SARDet-100K	57.31	87.44	61.99
		DOTA	38.47	75.81	32.82
	SM3Det	DroneVehicle	41.64	72.98	44.35
		Overall	45.25	78.97	45.07
		SARDet-100K	59.01	88.77	63.84
SARDet-100K: Retina DOTA: S <sup>2</sup> ANet DroneVehicle: S <sup>2</sup> ANet	individual models	DOTA	39.79	76.07	35.71
		DroneVehicle	45.13	75.92	50.65
		Overall	41.99	76.81	40.22
	SM3Det	SARDet-100K	51.08	82.50	55.27
		DOTA	38.47	75.81	32.82
		DroneVehicle	41.64	72.98	44.35
SARDet-100K: Retina DOTA: S <sup>2</sup> ANet DroneVehicle: S <sup>2</sup> ANet	individual models	Overall	43.13	77.62	42.67
		SARDet-100K	50.63	82.04	54.82
		DOTA	39.45	76.44	35.15
	SM3Det	DroneVehicle	45.15	75.83	50.67

Table S11. Performance comparison of SM3Det with individual models across various detector combinations.

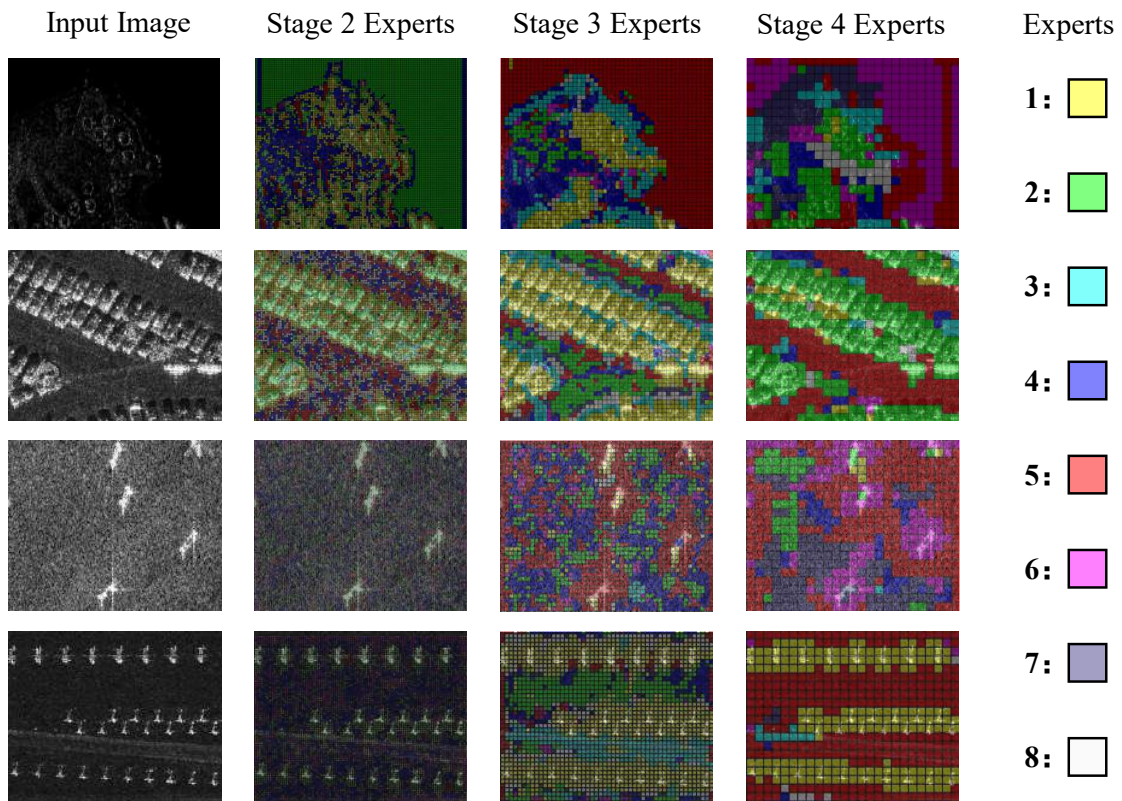


Figure S8. Visualization of grid-level expert activation across the last three stages of a well-tuned ConvNext-T backbone on SARDet-100K images. Each square grid represents the receptive field at a given stage, with different colours indicating the local grid areas processed by distinct experts. The top-1 selected experts for each grid are shown.

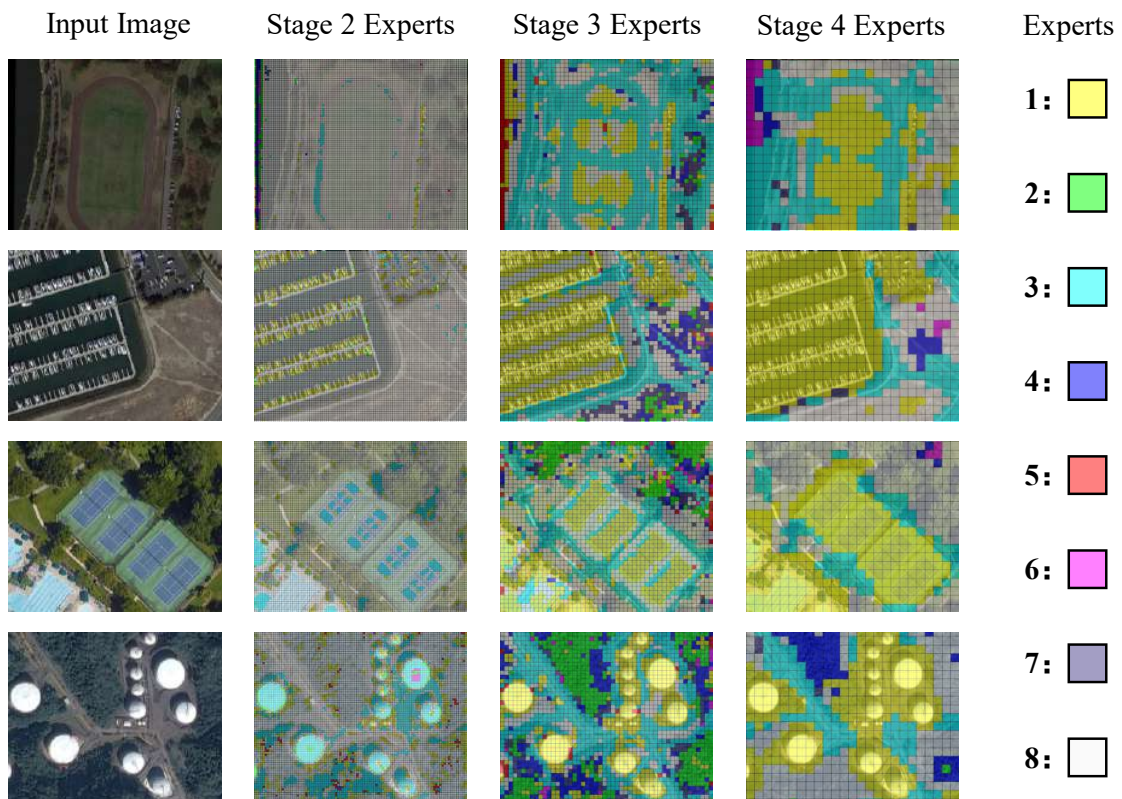


Figure S9. Visualization of grid-level expert activation across the last three stages of a well-tuned ConvNext-T backbone on DOTA-v1.0 images. Each square grid represents the receptive field at a given stage, with different colours indicating the local grid areas processed by distinct experts. The top-1 selected experts for each grid are shown.

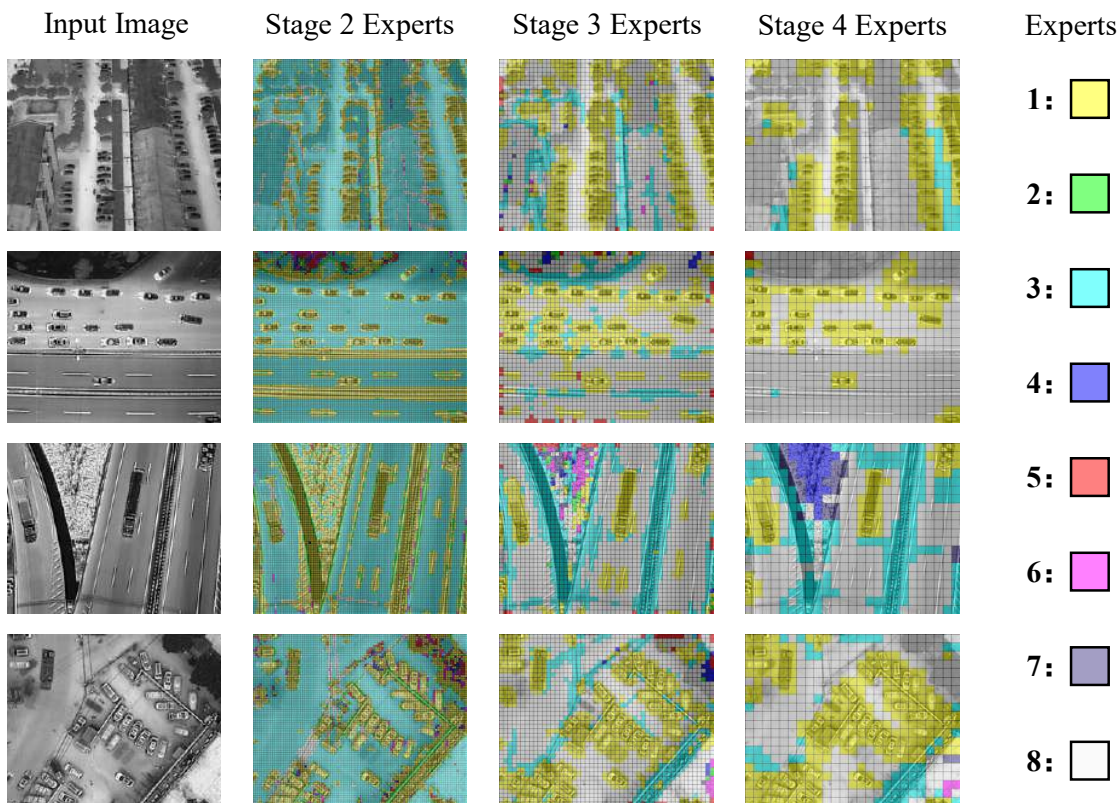


Figure S10. Visualization of grid-level expert activation across the last three stages of a well-tuned ConvNext-T backbone on DroneVehicle images. Each square grid represents the receptive field at a given stage, with different colours indicating the local grid areas processed by distinct experts. The top-1 selected experts for each grid are shown.

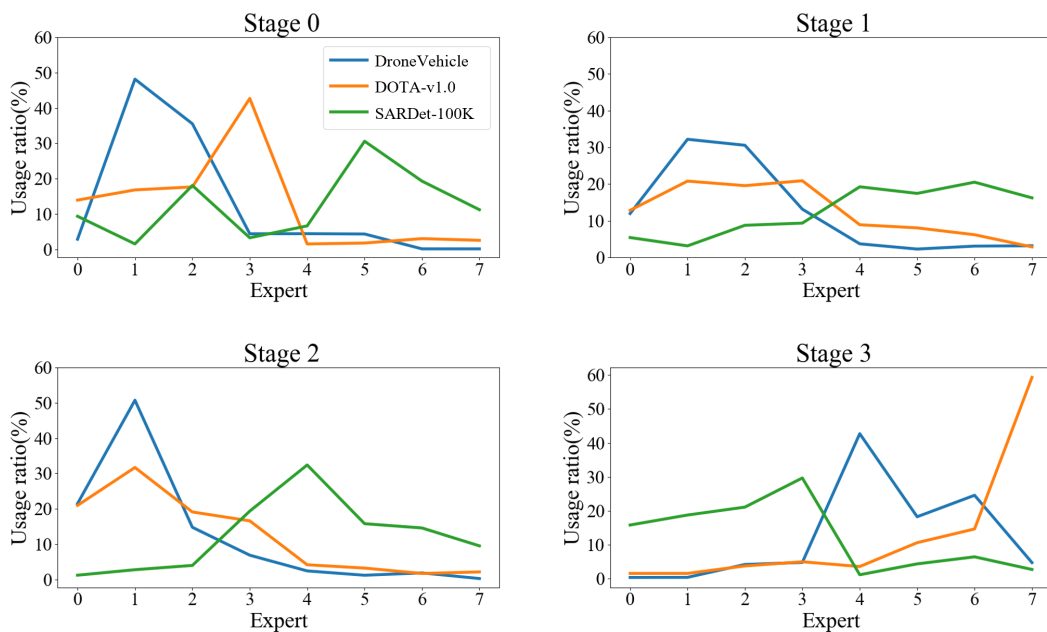


Figure S11. Expert participation statistics across SARDet-100K, DOTA, and DroneVehicle datasets. Some experts contribute to shared representation learning across all modalities, while others specialize in distinct patterns, activating only specific modalities.